Soft-x-ray laser scheme in a plasma created by optical-field-induced ionization of nitrogen

S. Hulin,[1,2] T. Auguste,[1] P. D'Oliveira,[1] P. Monot,[1] S. Jacquemot,[2] L. Bonnet,[2] and E. Lefebvre[2]
[1]*DSM/DRECAM/SPAM, CEA Saclay, 91191 Gif-sur-Yvette, France*
[2]*DAM/DIF/DPTA/SPPE, CEA/DAM en Ile de France, 91680 Bruyères-le-Chatel, France*
(Received 29 October 1999)

An x-ray laser scheme based on the recombination of a fully stripped nitrogen plasma is presented. Plasma is assumed to be created by the optical-field ionization of a nitrogen gas jet of 10^{19} cm^{-3} atomic density by an ultrashort (60 fs), high-intensity (3×10^{19} W/cm^2) Ti:sapphire laser. Results of two-dimensional particle-in-cell simulations, modeling laser-plasma interaction, parametric heating, and ponderomotive effects are presented. Hydrodynamic and kinetics calculations are performed and predict important local gain for H-like nitrogen transitions at 25 and 134 Å, following fast collisional recombination for specific plasma conditions.

PACS number(s): 42.55.Vc, 32.80.Rm, 52.50.Jm, 52.35.Mw

I. INTRODUCTION

With the development of the chirped pulse amplification technique and the improvement of Ti:sapphire technology, x-ray laser schemes based on fast collisional recombination of highly ionized plasmas seem achievable. Actually, tunnel ionization [so-called optical-field ionization (OFI)], first studied by Keldysh [1] for the hydrogen atom, is the predominant ionization process in high-intensity laser-matter interaction. It allows for the creation of a plasma composed of fully stripped ions and is characterized by a relatively low electronic temperature ($\sim$10 eV) for a linearly polarized [2] laser pulse. This cold electronic population is suitable for fast collisional recombination after the laser, resulting in a strong population inversion on the resonance line of H-like ions [3,4]. Lasing to the ground state allows to reach the shortest wavelength that can be expected from an electronic transition between two successive levels of an ion, which makes this scheme particularly attractive. Several groups around the world have demonstrated the feasibility of this scheme at 13.5 nm [5,6] but up to now, to the best of our knowledge, no other wavelength has been successfully amplified.

In this paper a detailed numerical study of an x-ray laser scheme based on the recombination of a fully stripped nitrogen plasma created by an ultrashort (60 fs), high-intensity (3×10^{19} W/cm^2) linearly polarized laser pulse is presented.

Since Peyraud *et al.* have considered the case of lasing down to the ground state, numerous theoretical [7] and numerical [8] works have been carried out. All these works have shown that the temperature must be kept low ($\sim$10 eV) and electron density high ($\sim10^{20}$ cm^{-3}) in order to obtain significant gain. Therefore the severe control of the temperature and density during the plasma creation constitutes the major difficulty of these schemes. The first heating source that must be considered here is the residual energy following OFI, i.e., the so-called above threshold ionization energy [2,9]. It is also well known that OFI happens in few optical cycles so that the main part of the pulse interacts with a highly ionized plasma. With an electron density of around 10^{20} cm^{-3} and high-intensity laser (3×10^{19} W/cm^2), parametric heating can be strong during the interaction and may even become the most important heating source. It is therefore of primary importance to study instabilities growth as ponderomotive effects that are likely to create suprathermic electrons as well as plasma channeling. The main consequence of the ponderomotive effects for the fast recombination laser scheme is the decrease of the plasma density along the propagation axis of both the driving and the x rays.

This paper is organized as following. In Sec. II we consider a plasma created by OFI of atomic nitrogen gas and we present calculations of the energy gained by the electrons due to the ionization process. Section III is devoted to two-dimensional (2D) particle-in-cell PIC) simulations which give information on electronic and ionic dynamics during the interaction, parametric instabilities, and ponderomotive effects. In Sec. IV we present results of atomic calculations performed with a kinetics code which is used as a postprocessor of a 1D$\frac{1}{2}$ hydrodynamic code. Initial conditions for the 1D$\frac{1}{2}$ hydrodynamic code are deduced from PIC simulations. Important local gains at 24.8 Å on Lyman α transitions and at 133.8 Å on Balmer α transitions of H-like nitrogen are calculated by this way and presented in this section. We discuss the different aspects of laser-plasma interaction and x-ray laser scheme and consider the interest of using a preionized medium in Sec. V. We summarize the main results and conclude in Sec. VI.

II. TUNNEL IONIZATION OF NITROGEN

For laser parameters considered herein ($I=3\times10^{19}$ W/cm^2, $\tau=60$ fs, $\lambda=0.8$ μm), the ionization of gases is due to OFI and is well described [10,11] by Ammosov, Delone, and Krainov (ADK) [12] rates. Time dependence of the average charge state for a Gaussian laser pulse of 60 fs full width at half maximum (FWHM) duration, $I_{max}=3\times10^{19}$ W/cm^{-2} at $\lambda=0.8$ μm, interacting with atomic nitrogen is represented in Fig. 1. The dashed line corresponds to the pulse shape. We can see that the five

 ©2000 The American Physical Society

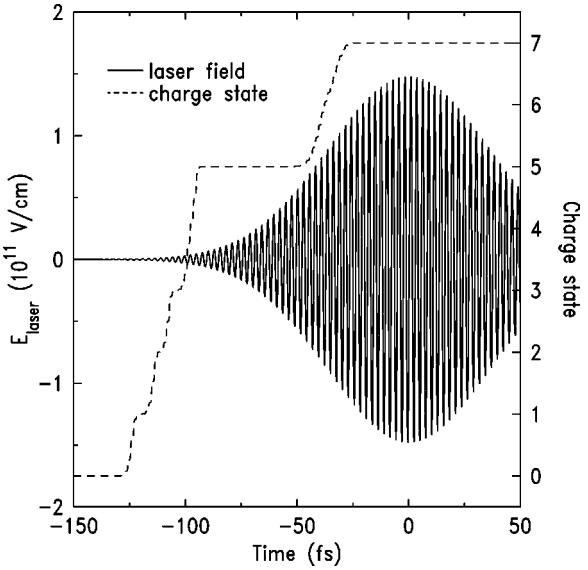

FIG. 1. Average charge state of nitrogen (dashed line) and electric laser field (full line) vs time. The laser is assumed to have a Gaussian shape of 60 fs FWHM duration with 3×10^{19} W/cm^2 maximum intensity at 0.8 μm wavelength.

external shell electrons are ionized during the very first part of the pulse in a few optical cycles. The binding electric field of these levels is in the 5×10^{9}–5×10^{11} V/cm range. When the laser field reaches 10% of the binding field, ADK ionization rates are already 10^{15}–10^{16} s^{-1}. This explains why nitrogen is five times ionized so early with respect to the time of maximum intensity. Only a few optical cycles are necessary to go from one charge state to the following one. It is more difficult to release the last two inner shell electrons because their binding energy (552 eV and 667 eV, respectively) is five times higher than the binding energy of the most outer bound shell electron (98 eV). An energy of 667 eV is equivalent to a binding electric field of 1.7×10^{12} V/cm. We can then suppose (and it will be confirmed in the following paragraph) that nitrogen will be fully ionized for a laser field of approximately 1.7×10^{11} V/cm (10% of the binding field).

Because the ground state of the H-like ion must be as empty as possible for the x-ray laser scheme [4,7,8], it is important to know the saturation intensity. This quantity can be defined as the intensity over which the occupancy number of an ion is below 10^{-4}. Because of the strong dependence of the ADK ionization rates with the laser intensity ($W_{ADK}\propto I^7$ [11]), the occupancy number of one ionization state increases very rapidly with increasing intensity (see Fig. 2). We can say from this figure that the saturation intensity is between 2×10^{19} and 3×10^{19} W/cm^2 for H-like nitrogen. We can then consider that nitrogen is fully ionized if the laser intensity is greater than 3×10^{19} W/cm^2 (i.e., around 10% of the electric binding field as previously predicted).

In the tunnel ionization process, the energy effectively gained by an electron released by an ion in the laser field depends on the phase mismatch between the time of the laser field maximum and the time of the ejection. The resulting energy, for a linearly polarized laser, can be estimated as follows

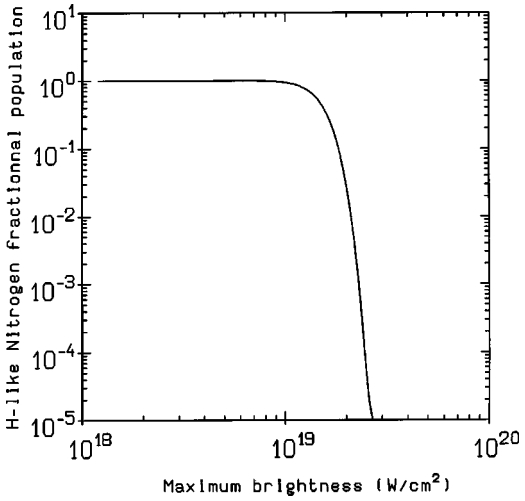

FIG. 2. Fraction of H-like nitrogen ions in the ground state as a function of the maximum laser intensity. The laser pulse is always assumed to have a Gaussian shape of 60 fs FWHM duration at 0.8 μm wavelength.

$$\langle E_{ATI}\rangle = 2U_p\left|\frac{\sum_{j=1}^{Z_{max}}\int_0^{t_{max}}\exp(-t/\tau_p)^2 n_{j-1}(t)W_j\cos^2(w_0t)dt}{\sum_{j=1}^{Z_{max}}\int_0^{t_{max}} n_{j-1}(t)W_j dt}\right|,$$

where $U_p=(e^2E^2)/(4m_e\omega_0^2)$ is the ponderomotive potential. Because U_p varies very rapidly, $[U_p(t)\propto I(t)]$,$E_{ATI}(t)$ is strongly dependent on the time of ionization. Characteristic time of ionization of a specific ion τ_k (with $k=1$ to 7) is, however, short in comparison with the pulse duration τ_p: $\tau_k\sim1$ fs$\ll\tau_p=60$ fs. For these reasons each of the seven electron populations can be characterized by its *own* temperature [13]:

$$3\ \text{eV}\leqslant T_{e,k}\leqslant 120\ \text{eV}\ \text{ for }\ k=1\ \text{ to }\ 5,$$

$$T_{e,k}\sim 50\ \text{keV}\ \text{ for }\ k=6,7.$$

These temperatures are only relevant as long as no collision occurs between an appearing population and the free electrons already present in the plasma. Electron-electron collision time $\tau_{e-e,k}$ has to be carefully evaluated following the Spitzer and Härm formula [14] with the corresponding $T_{e,k}$. It becomes

$$60\ \text{fs}\leqslant\tau_{e-e,k}\leqslant 2.6\ \text{ps}\ \text{ for }\ k=1\ \text{ to }\ 5,$$

$$\tau_{e-e,k}\sim 13\ \text{ns}\ \text{ for }\ k=6,7.$$

There is a significant difference between the outer shell electrons and the *K* shell ones. As the population inversion happens during the first ps of recombination (see Sec. IV), only the five first electron populations have interacted. The relevant plasma temperature is then an average over the five first electron population temperatures:

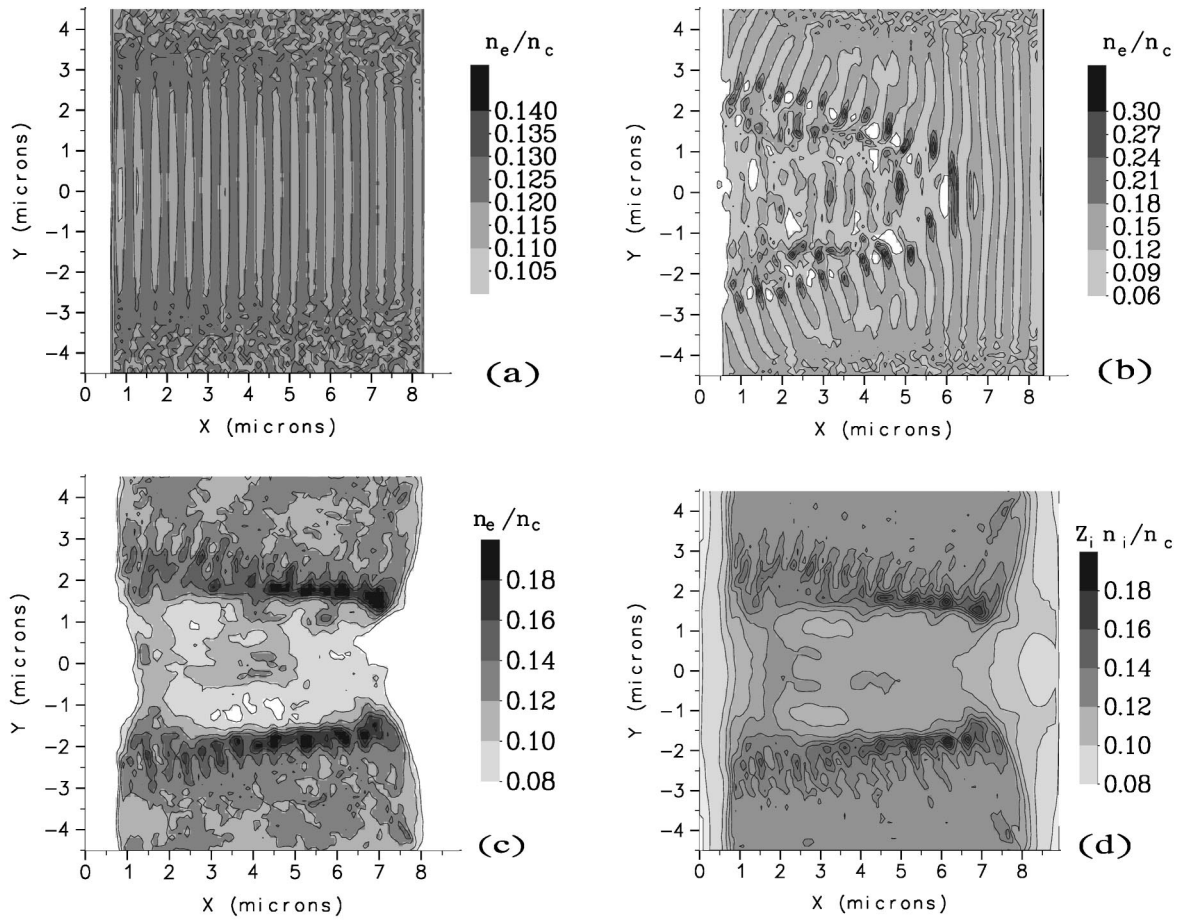

FIG. 3. 2D plots of the electronic (a), (b), (c) and ionic (d) densities versus X (propagation direction of the laser) and Y (polarization direction of the laser) for three different times: 46 fs (a) and 16 fs (b) before the maximum of the laser pulse and 222 fs (c), (d) after the maximum of the laser pulse. The laser is 60 fs FWHM with 3×10^{19} W/cm^2 maximum intensity. It propagates from the left to the right of the figure in an initially 2×10^{20} cm^{-3} homogeneous $N^{7+}-e^-$ plasma.

$$T_e=\frac{\sum_{k=1}^{5} n_k T_{e,k}}{\sum_{k=1}^{5} n_k}=45 \text{ eV}.$$

The hot electrons, issued from K-shell ionization, do not contribute to plasma heating on the first ns.

Detailed study of the ionization process has shown that it is possible, with a few 10^{19} W/cm^2 laser pulses of 60 fs duration, to create a fully ionized nitrogen plasma and that the amount of energy coming from the ionization process is less than 45 eV during the first ns after interaction.

III. PIC SIMULATIONS

After having ionized the gas in its rising edge, the main part of the laser pulse interacts with a highly ionized nitrogen plasma. If the initial pressure of the atomic nitrogen gas is around 1 atm, the electron density n_e after complete ionization is around 10% of the critical density n_c. In this range of parameters ponderomotive and relativistic effects are indeed very strong and parametric instabilities can play an important role. To study these processes we performed simulations with the Cartesian 2D-PIC code MANET which solves collisionless Vlasov equations for particles coupled to Maxwell equations for the electromagnetic fields. The laser is defined as being linearly polarized along the y axis and is propagated along the x axis. Temporal and spatial profiles of the laser pulse are assumed to have Gaussian shapes of $140\omega_0^{-1}$ FWHM (60 fs) and $19k_0^{-1}$ FWHM (2.5 μm), respectively. The maximum intensity is reached $250\omega_0^{-1}$ (106 fs) after the beginning of the simulation. The plasma is $60k_0^{-1}$ (7.8 μm) long and $76.8k_0^{-1}$ (10 μm) large while the simulation box is 70 k_0^{-1} (9.1 μm) long and $76.8k_0^{-1}$ (10 μm) large. The time step is $0.02\omega_0^{-1}$ and the cells are $0.04k_0^{-1}\times0.04k_0^{-1}$. The small dimensions of the simulation are due to the low initial plasma temperature. Following the precedent section it was assumed to be 45 eV. The plasma is composed of electrons and N^{7+} ions and there are five particles of each species per plasma cell leading to a 28 800 000 total number of particles.

We have plotted in Fig. 3 the electron density profile for three different times (a),(b),(c) as well as the ionic density profile at the end of the simulation (d). The first effect produced by the laser on the plasma is a perturbation of the electron density with a $\lambda_0/2$ characteristic scale length [Fig. 3(a)]. It can be related to the $2\omega_0$ component of the ponderomotive force which appears when one calculates the motion of one electron in a strong laser field at the second order for

the fields and the speed of the electron:

$$m_e \frac{d\vec{v}}{dt} = -e\vec{E}_1 \cos(\omega_0 t - \vec{k}_0 \cdot \vec{r}) - \frac{e^2}{4m_e\omega_0^2}\vec{\nabla}(\vec{E}_1^2)\{1-\cos[2(\omega_0 t - \vec{k}_0 \cdot \vec{r})]\}.$$

$\vec{E}_1$ is the slowly varying component of the laser electric field. Because of the strength of the electric field gradient, a large number of the electrons oscillate, leading to electron density modulations at $2\omega_0$ frequency.

The ejection of electrons by the unmodulated component of the ponderomotive force (the ''usual'' ponderomotive force) is very clear in Fig. 3(b). They are ejected from the propagation axis to the edges with a $\pm 30°$ angle with respect to the direction of propagation of the laser, with energies up to 7 MeV. However, they do not simply follow the intensity gradient. The $2\omega_0$ component overimposed on the usual component produces a series of electron bunches and holes modulated at $\lambda_0/2$. The amplitude of these modulations can reach 100% of the electron density in the region where the electric field gradient is maximum [Fig. 3(b)]. Then, after the laser cutoff, an electron density channel is formed [see Fig. 3(c)]. It lasts till the end of the simulation in the case of nitrogen because the ions are light enough to start moving under the space charge effect created by the electronic depletion which happens during the interaction. The density profile of the N^{7+} ions after the laser is shown in Fig. 3(d). It is really close to the electron density profile at the same time [see Fig. 3(c)]. Furthermore ions do not stop immediately after the laser because of their inertia. They keep on moving away from the propagation axis to the edges with an average speed of 3×10^8 cm$\times$s^{-1}. Thus a plasma channel is formed which later evolution is driven by the equations of hydrodynamics. The plasma depletion can reach 20% of the initial density and is bounded by plasma walls whose average density is between 20% and 100% higher than the initial density. Fortunately, the plasma depletion is limited and therefore does not prevent the x-ray laser scheme from working. Furthermore, it could play an important role in guiding the x rays but this aspect of the problem is beyond the scope of this paper.

Electrons that are ejected by the ponderomotive force do not contribute to the heating of the channel. However, an average electronic temperature of 900 eV is obtained after the laser cutoff. It can be explained by the backward stimulated Raman scattering (BSRS) detected in the time integrated spectrum of the E_y electric field measured at the left side (entrance side) of the simulation box. This spectrum is presented in Fig. 4 where the Stokes component of the BSRS at $\omega_0 - \omega_p$ is clearly identified. Estimation of its growth rate γ_{BSRS} can be performed as follows [16]:

$$\gamma_{BSRS} = \frac{\sqrt{3}^3}{2}\sqrt{\frac{n_e}{4n_c}}\, a_0^{2/3} k_0,$$

where $a_0 = E/E_c = 0.85\sqrt{I(10^{18}\ \mathrm{W/cm^2})\lambda^2(\mu\mathrm{m})}$ is the normalized electric field. With a pulse length $L_{pulse} = 26k_0^{-1}$, $a_0 = 2.15$, and $n_e/n_c = 0.12$ it becomes

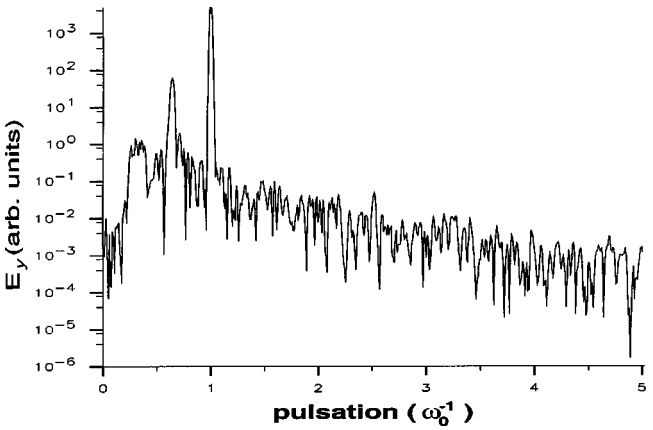

FIG. 4. Fourier transform of the time evolution of the transverse electric field E_y on the left side of the simulation box (in the backward direction).

$\gamma_{BSRS} L_{pulse} \approx 40$. This suggests that the Raman instability is especially strong despite the briefness of the pulse. Assuming that all the energy of the scattering plasma waves is transferred to the electrons of the plasma, the maximum possible temperature can be estimated by [15] $T_e = 1/12(n_e/n_c)(\delta n/n_0)^2 m_e c^2$ where δn is the plasma wave amplitude and n_0 the initial plasma density. With $n_e/n_c = 0.12$ and $\delta n/n_0 = 0.2$, $T_e \sim 1$ keV which is consistent with the average 900 eV obtained with the simulations. This may explain the high temperature of the electrons in the plasma channel just after the laser cutoff.

IV. HYDRODYNAMIC AND ATOMIC SIMULATIONS

Four specific features of the tunnel ionization compared to other ionization processes make it an interesting tool for x-ray lasing. First, the wavelength that can be achieved is the shortest that can be expected from a $\Delta n = 1$ transition in a given ion species, n being the principal quantum number. In fact, the energy of a level scales as $1/n^2$ so that the wavelength of a transition decreases with n. For instance, a $n = 2$ to $n = 1$ transition wavelength is five times shorter than a $n = 3$ to $n = 2$ one.

The second advantage of OFI is the emptiness of the lower level of the lasing transition. It means that the local gain coefficient can be extremely high as shown by Jones and Ali [7], for example (over 1000 cm^{-1}).

Third, the efficiency of tunnel ionization is so strong that 100% of the ions can be considered in the same charge state inside all the volume where the laser intensity is greater than the saturation intensity of the considered charge state. Thus, all the ions in this volume are in the same charge state with an occupancy number of all their levels (including the ground state) equal to zero. This is of primary importance for lasing to the ground state.

The fourth advantage of OFI is the release of an electron directly from its ground state to the continuum without excitation processes.

All these specificities of OFI make it a promising way of creating a plasma where the amplification of a transition in the x-rays range could occur.

The use of a high-intensity linearly polarized laser to create a plasma aims at obtaining a cold plasma whose recom-

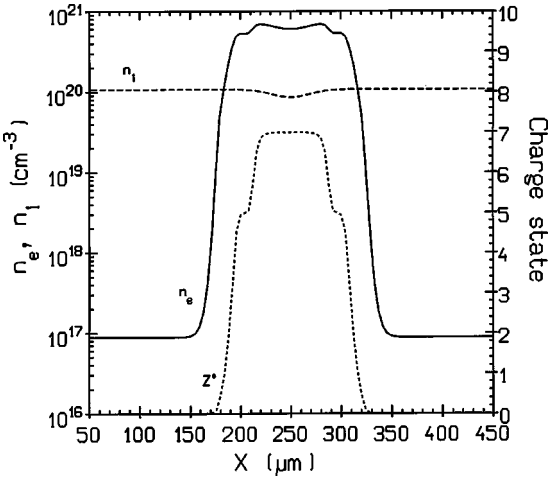

FIG. 5. Initial conditions of the hydrodynamic simulation versus space: electron density n_e (—), ionic density n_i (– –), and average charge state $Z^\star$ (. . .).

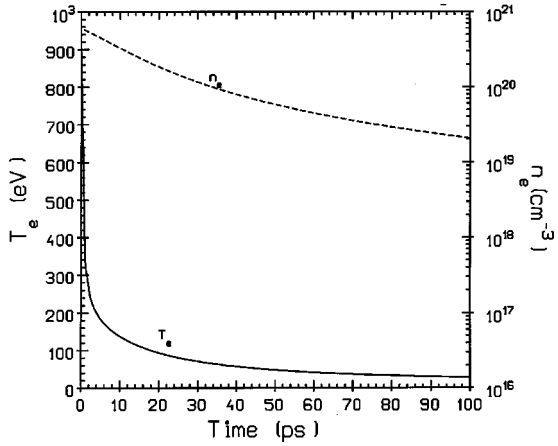

FIG. 6. Electronic temperature T_e (—) and density n_e (– –) versus time for an initial electron density of 6×10^{20} cm^{-3} and a temperature of 900 eV.

bination will be dominated by collisional processes. Actually, collisional recombination preferentially populates the high energy levels while radiative recombination fills the low energy ones and especially the ground state. The radiative recombination rate of Seaton [18] scales as $N_eZ(I_n/T_e)^{3/2}\mathcal{E}_1(I_n/T_e)\exp(I_n/T_e)$, where I_n is the energy of the level n, $\mathcal{E}_1$ is the exponential integral function, and Z is the charge state of the recombined ion. The collisional recombination rate of Lotz [19] scales as $N_e^2g_nT_e^{-3/2}\mathcal{E}_1(I_n/T_e)\exp(I_n/T_e)/(I_n/T_e)$, where g_n is the statistical weight of the level n. It emerges that the ratio of the collisional rate over the radiative rate scales as $(g_nN_e)/(Z\sqrt{T_e}E_n^{5/2})$. Thus, to enhance the process that populates the high energy levels without filling the low energy ones, a low temperature and a high density plasma is necessary.

Detailed kinetics simulations have been performed to calculate the recombination of a fully stripped nitrogen plasma and confirm the previous result. The LASIX [17] code was used as a postprocessor of the hydrodynamic code CHIVAS [20]. This latter provides the temporal evolution of the hydrodynamic parameters (temperature, density) following the plasma expansion. The initial conditions used to start hydrodynamic simulations are deduced from Sec. II (OFI) and Sec. III (PIC simulations) and are represented in Fig. 5. We took a flat atomic nitrogen density profile of 400 μm size in the $1\times10^{17}-1\times10^{20}$ cm^{-3} range. A channel with a Gaussian shape of 50 μm FWHM was assumed at the center of the density profile. In this channel the density is 20% less than the density of the surrounding plasma. The ionization degree of nitrogen is calculated for a collisional radiative equilibrium following an ionization temperature profile which has a Gaussian shape of 50 μm FWHM starting from 1 eV in the edges up to 700 eV at the center. The resulting electron density profile is a near top hat shape of 120 μm with a maximum in the $1\times10^{18}-1\times10^{21}$ cm^{-3} range. Initial ionic and electronic temperature profiles also have a Gaussian shape of 50 μm FWHM with a maximum in the 15–900 eV range. This plasma freely expands in vacuum and the postprocessor LASIX is used for the cell corresponding to the center of the hydrodynamic simulation. Cooling of this cell is represented in Fig. 6 for an initial electron density of 6×10^{20} cm^{-3}, an initial temperature of 900 eV, and a limiting flux factor of 0.03.

All the nonstimulated atomic processes are included in LASIX, i.e., collisional ionization, three-body recombination, collisional excitation and deexcitation, spontaneous emission, radiative recombination, dielectronic recombination, autoionization, resonant capture, and Auger ionization. H-like nitrogen energy levels as well as radiative deexcitation rates and collision strengths are calculated with the SUPERSTRUCTURE [21] code.

Two transitions following Lyman α lines and three transitions following Balmer α lines are potential candidates for lasing. Lyman α lines correspond to $2p_{1/2}\rightarrow1s_{1/2}$ and $2p_{3/2}\rightarrow1s_{1/2}$ transitions at both 24.78 Å and Balmer α lines correspond to $3d_{3/2}\rightarrow2p_{1/2}$, $3d_{3/2}\rightarrow2p_{3/2}$ and $3d_{5/2}\rightarrow2p_{3/2}$ transitions at 133.74 Å, 133.88 Å, and 133.87 Å, respectively. Results of local gains on the $n=2$ to $n=1$ transitions at 24.78 Å are first presented.

For an initial temperature of 15 eV and an electron density of 6×10^{20} cm^{-3}, local gain coefficients up to 1100 cm^{-1} for the $2p_{3/2}\rightarrow1s_{1/2}$ transition and 450 cm^{-1} for the $2p_{1/2}\rightarrow1s_{1/2}$ transition (see Fig. 7) are predicted. The gain duration is of the order of 1 ps, and because the statistical weight of the $2p_{3/2}$ level is twice the $2p_{1/2}$ one, the gain coefficient of the $2p_{3/2}\rightarrow1s_{1/2}$ is always two times greater than the gain coefficient of the $2p_{1/2}\rightarrow1s_{1/2}$ transition. Figure 8 shows the evolution with temperature of the maximum local gain coefficient G_{max} of the $2p_{3/2}\rightarrow1s_{1/2}$ transition for several densities. A strong dependence, scaling as $\exp(-kT_e)$, of G_{max} with T_e can be observed. For a density of 6×10^{20} cm^{-3}, G_{max} drops from 1100 cm^{-1} for a temperature of 15 eV down to 2 cm^{-1} for a temperature of 50 eV. Whatever the density is, the variation of G_{max} with temperature is always the same and emphasizes how precise the control and knowledge of the plasma temperature must be.

Even if the variation of gain coefficient with density is smoother, it nevertheless scales as N_e^3, as shown in Fig. 9. For instance, for a 25 eV plasma, G_{max} increases from less than unity for a density of 3×10^{20} cm^{-3} up to 100 cm^{-1} for a density of 6×10^{20} cm^{-3}. Thus, to obtain stimulated emis-

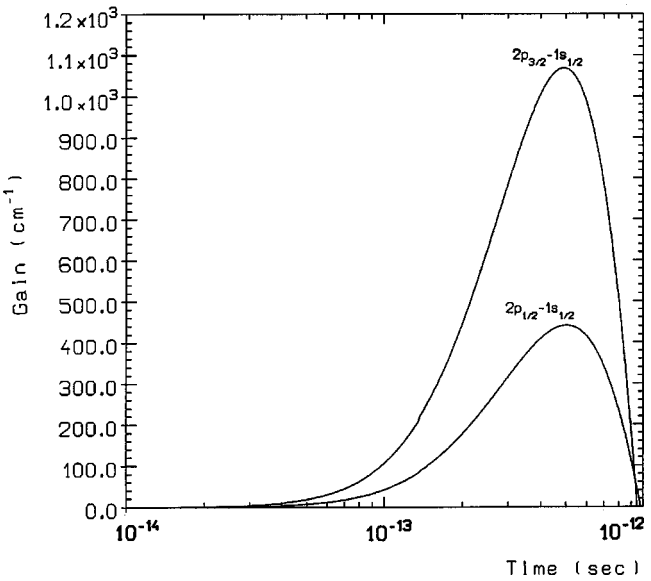

FIG. 7. Time dependence of the local gain coefficient for the $2p_{3/2}\rightarrow 1s_{1/2}$ and the $2p_{1/2}\rightarrow 1s_{1/2}$ transitions ($\lambda = 24.78$ Å) for optimal plasma conditions: $T_e = 15$ eV and $N_e = 6\times 10^{20}$ cm^{-3}.

sion between the $n=2$ and $n=1$ levels of H-like nitrogen, it is necessary to create a plasma whose electronic temperature is below 50 eV and whose electron density is over a few 10^{20} cm^{-3}.

During the recombination phase, some transitions between $n=3$ and $n=2$ levels also exhibit population inversion. They are the $3d_{3/2}\rightarrow 2p_{1/2}$, $3d_{3/2}\rightarrow 2p_{3/2}$, and $3d_{5/2}\rightarrow 2p_{3/2}$ transitions at 133.74 Å, 133.88 Å, and 133.87 Å, respectively. For a low temperature and/or a high density, the inversion dynamics is the same as the $n=2$ to $n=1$ inversion one. Because the $n=2$ level is initially empty and because radiative recombination on levels $n=2$ is slower than collisional recombination on levels $n=3$, a strong and transient lasing can occur ($G_{max} = 1370$ cm^{-1} for the $3d_{5/2}\rightarrow 2p_{3/2}$ transition at 15 eV and 6×10^{20} cm^{-3}, duration <1 ps). However, for a higher temperature and/or a smaller density, lasing following the *classical* recombination scheme

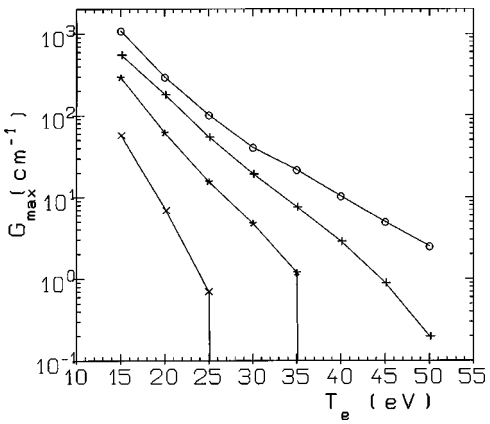

FIG. 8. Maximum local gain of the $2p_{3/2}\rightarrow 1s_{1/2}$ transition ($\lambda = 24.78$ Å) as a function of the temperature for several densities: 6×10^{20} cm^{-3} (○), 5×10^{20} cm^{-3} (+), 4×10^{20} cm^{-3} (⋆), 3×10^{20} cm^{-3} (×).

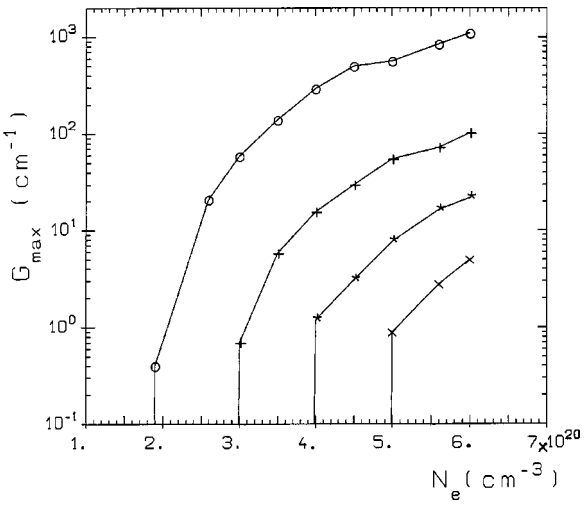

FIG. 9. Maximum local gain of the $2p_{3/2}\rightarrow 1s_{1/2}$ transition ($\lambda = 24.78$ Å) as a function of the density for several temperatures: 15 eV (○), 25 eV (+), 35 eV (⋆), 45 eV (×).

can also be achieved. Actually, even if the radiative recombination on level $n=2$ is stronger than the collisional recombination on level $n=3$, the occupancy rate of level $n=2$ can be less than the occupancy rate of level $n=3$. This is because of the high radiative deexcitation rate of level $n=2$ to level $n=1$ following the resonant $2\rightarrow 1$ transition. This change in dynamics is illustrated by Fig. 10 for the $3d_{5/2}\rightarrow 2p_{3/2}$ transition which is the most intense one. For an initial temperature of 40 eV and an initial electron density of 5×10^{20} cm^{-3}, gain starts immediately and lasts 0.5 ps, whereas for the same initial temperature and an initial electron density of 1×10^{19} cm^{-3}, gain starts a few ps after the beginning of the recombination and lasts hundreds of ps.

A major point in the change of dynamics is that lasing duration and time of occurrence are mainly dependent on the

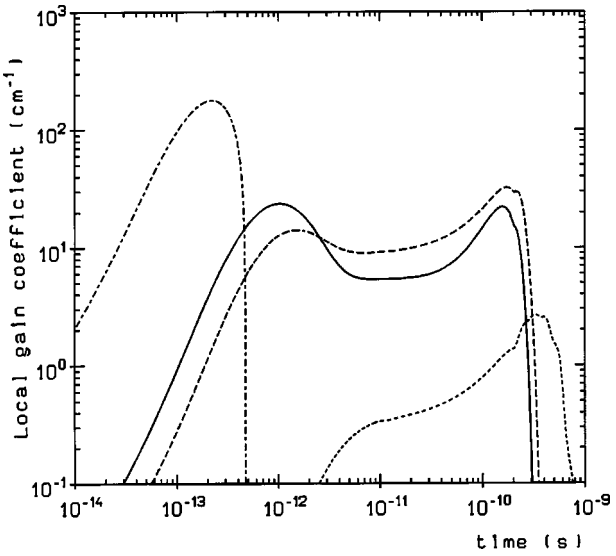

FIG. 10. Time evolution of the local gain coefficient of the $3d_{5/2}\rightarrow 2p_{3/2}$ transition for an initial temperature of 40 eV and four different initial densities: $n_e = 1\times 10^{19}$ cm^{-3} (- - -), $n_e = 7.5\times 10^{19}$ cm^{-3} (– –), $n_e = 1\times 10^{20}$ cm^{-3} (—), $n_e = 5\times 10^{20}$ cm^{-3} (– -).

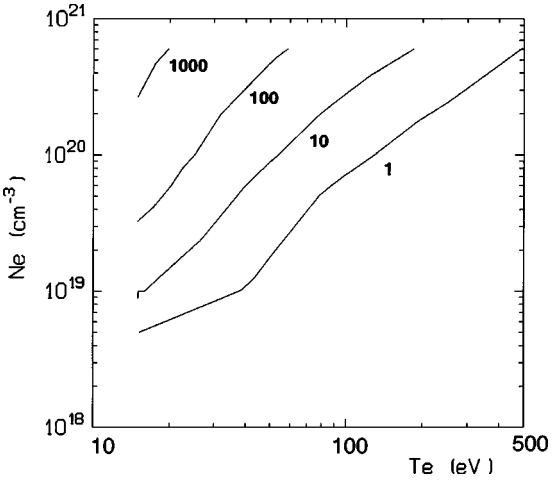

FIG. 11. Maximum local gain coefficient G_{max} (in cm^{-1}) of the $3d_{5/2} \rightarrow 2p_{3/2}$ transition versus initial electronic temperature and density.

hydrodynamic of the expansion. As is the case for the laser-solid recombination x-ray laser schemes, it is not the initial temperature but the cooling speed that is the key parameter. Thus, even if the initial temperature of the plasma is around 100 eV, the stimulated emission happens when the plasma temperature has dropped to tens of eV. In Fig. 11 is represented the maximum local gain coefficient versus initial temperatures and densities for the $3d_{5/2} \rightarrow 2p_{3/2}$ transition. For initial densities over 10^{19} cm^{-3} and/or initial temperatures below 100 eV, a population inversion between the $3d_{5/2}$ level and the $2p_{3/2}$ level can be obtained, whereas for a $n=2 \rightarrow n=1$ transition, population inversion occurs for densities greater than 10^{20} cm^{-3} and initial temperatures below 50 eV. The range of parameters for which a $n=3 \rightarrow n=2$ population inversion can be generated is then much wider than for a $n=2 \rightarrow n=1$ population inversion.

V. DISCUSSION

An x-ray laser experiment is based on the creation of a varying length medium in order to measure the intensity variation with length and deduce the gain-length product. This supposes the possibility of generating a long enough medium where intensity is over the saturation intensity (see Sec. II). This length is directly connected to the propagation properties of the short pulse, which is limited to the Rayleigh range in the case of a classical focusing. To create this long medium we propose to use relativistic self-focusing. Several experiments [22–24] have indeed shown that for laser power above the critical power for self-focusing P_c, it is possible to guide a multiterawatt laser pulse over several Rayleigh ranges. With a density of 10^{20} cm^{-3}, a power of 10 TW is 70 times higher than the critical power P_c for relativistic self-focusing. To enhance self-focusing on the one hand and to avoid defocusing effects due to the plasma ionization in the rising edge of the driving pulse [25] on the other hand, it is better to use a low power, long duration laser pulse to create a cold and partially ionized preplasma. Simulations with the 1D hydrodynamic code CHIVAS have been performed to study the preionization phase. These simulations have shown that the use of a 10 ns Nd:yttrium-aluminum-garnet laser of few hundreds of mJ, focused on a 100 μm diameter focal spot, may lead to the creation of a N^{5+} plasma at a temperature below 30 eV. However, with classical focusing optics, the length of the preionized medium will be limited to, or even shorter than, the Rayleigh range. In that case, the interaction length is mainly limited by inverse bremsstrahlung absorption of the nanosecond laser by the high pressure gas. On the other hand, it was recently demonstrated that the use of an axicon is well adapted to generate a long scale plasma [26]. Thus, the short pulse interacts with a partially ionized plasma, which prevent ionization-induced refraction.

In the hydrodynamic simulations performed to simulate the plasma expansion, the initial speed of the plasma channel walls, given by the PIC simulations, was not taken into account. In fact, in the CHIVAS and LASIX simulations of Sec. IV, the plasma is assumed to be initially at rest while the PIC code gives a radial expansion velocity of the plasma walls of 10^8 $cm \times s^{-1}$. This initial speed should enhance the plasma expansion and, therefore, its cooling. This point does not concern the $2 \rightarrow 1$ population inversion at 24.78 Å but is very interesting for the $3 \rightarrow 2$ population inversion at 133.87 Å where the plasma cooling rate is a major parameter as explained in Sec. IV. Only a few simulations where this initial speed is taken into account have been performed. They effectively show an increase in the cooling speed and the gain on $n=3$ to $n=2$ transitions is enhanced. Further simulations are now in progress to confirm this point.

Another major parameter in the modeling of the OFI x-ray laser scheme is the shape of the electron distribution function. Previous works [3,4,7,8] and the present one assume a Maxwellian distribution function to calculate the various rates in the atomic kinetics model. However, the distribution function of OFI plasmas is far from being a Maxwellian and presents an important amount of cold electrons [2]. Equilibration to a Maxwellian of this function is not very well understood yet and its influence on the different collisional rates, and finally on the gain, is not well described despite several pioneering works on the subject [27,28]. This is mainly related to the complexity of coupling a Fokker-Planck code with a kinetic one. This specificity of the OFI ionization may play a crucial role in the present scheme because of the short time between the beginning of the recombination and the time for population inversion between the $2p_{3/2} \rightarrow 1s_{1/2}$ levels (<1 ps).

VI. CONCLUSIONS

An x-ray laser scheme based on the OFI ionization of nitrogen gas was presented. The plasma creation by focusing a 60 fs, 3×10^{19} W/cm^2, 800 nm laser pulse in a pulsed gas jet of atomic nitrogen was studied and it was shown that a fully stripped nitrogen plasma can be created. Laser-plasma interaction was numerically investigated using a 2D-PIC code. It was found that the Raman instability can be an important heating source for the electrons of the plasma. Temperatures up to 900 eV were found. It was also shown that the ponderomotive effects lead to the creation of a plasma channel with a density 20% lower than the one of the sur-

rounding plasma. The ponderomotive force also gives rise to the ejection of suprathermic electrons with energy up to 7 MeV. The recombination phase following plasma expansion in vacuum was also considered. Detailed atomic calculations have shown that stimulated emission at 25 Å can be expected for very low temperature (<50 eV) and high density ($>10^{20}$ cm^{-3}) plasmas whereas stimulated emission at 134 Å is expected to occur in a wider range of temperatures (<100 eV) and densities ($>10^{19}$ cm^{-3}).

[1] L.V. Keldysh, Zh. Éksp. Teor. Fiz. **47**, 1945 (1964) [Sov. Phys. JETP **20**, 1307 (1965)].

[2] P.B. Corkum, N.H. Burnett, and F. Brunel, Phys. Rev. Lett. **62**, 1259 (1989).

[3] L.A. Shelepin and L.I. Gudzenko, Dokl. Akad. Nauk. (SSSR). **160**, 1296 (1965) [Sov. Phys. Dokl. **10**, 147 (1965)].

[4] Y.J. Peyraud and N. Peyraud, J. Appl. Phys. **43**, 2993 (1972).

[5] Y. Nagata, K. Midorikawa, S. Kubodera, M. Obara, H. Tashiro, and K. Toyoda, Phys. Rev. Lett. **71**, 3774 (1993).

[6] D.V. Korobkin, C.H. Nam, S. Suckewer, and A. Goftsov, in *Proceedings of the 5th International Conference on X-ray Lasers, Lund Sweden, June 1996*, edited by S. Suanberg and C. G. Wahlström, IOP Conf. Proc. No. 151 (Institute of Physics and Physical Society, London, 1996), Sec. 4, p. 151.

[7] W.W. Jones and A.W. Ali, Appl. Phys. Lett. **26**, 450 (1975).

[8] P.A. Amendt, D.C. Eder, and S.C. Wilks, Phys. Rev. Lett. **66**, 2589 (1991).

[9] N.B. Delone and V.P. Krainov, J. Opt. Soc. Am. B **8**, 1207 (1991).

[10] S. Augst, D. Strickland, and D.D. Meyerhofer, Phys. Rev. Lett. **63**, 2212 (1989).

[11] T. Auguste, P. Monot, and L.A. Lompré, J. Phys. B **25**, 4181 (1992).

[12] M.V. Ammosov, N.B. Delone, and V.P. Krainov, Zh. Éksp. Teor. Fiz. **91**, 2008 (1986) [Sov. Phys. JETP **64**, 1191 (1986)].

[13] N.E. Andreev, M. Chegotov, M.E. Veĭsman, T. Auguste, P. D'Oliveira, S. Hulin, P. Monot, A.Y. Faenov, T.A. Pikuz, A.I. Magunov, I.Y. Skobelev, F.B. Rosmej, and M.Y. Romanovskiĭ, Pisma. Zh. Éksp. Teor. Fiz. **68**, 577 (1998) [JETP Lett. **68**, 582 (1998)].

[14] L. Spitzer, Jr. and R. Härm, Phys. Rev. **89**, 977 (1953).

[15] V.I. Kirsanov and S.A. Sakharov, Plasma Phys. Rep. **21**, 623 (1995).

[16] N.E. Andreev V.I. Kirsanov, and L. M. Gorbanov, Phys. Plasmas **2**, 2573 (1994).

[17] E. Berthier, Rapport des Activités Laser No. CEA/CEL-V, 1998 (unpublished).

[18] M.J. Seaton, Mon. Not. R. Astron. Soc. **119**, 81 (1959).

[19] W. Lotz, Z. Phys. **220**, 466 (1969).

[20] S. Jacquemot and A. Decoster, Laser Part. Beams **9**, 517 (1991).

[21] W. Eissner, M. Jones, and H. Nussbaumer, Comput. Phys. Commun. **8**, 270 (1974).

[22] T. Auguste, P. Monot, G. Mainfray, C. Manus, S. Gary, and M. Louis-Jacquet, Opt. Commun. **105**, 292 (1994).

[23] A.B. Borisov, V.V. Korobkin, A.M. Prokhorov, C.K. Rhodes, and O.B. Shiryaev, Phys. Rev. Lett. **65**, 1753 (1990).

[24] P. Monot, T. Auguste, P. Gibbon, F. Jakober, G. Mainfray, A. Dulieu, M. Louis-Jacquet, G. Malka, and J-L. Miquel, Phys. Rev. Lett. **74**, 2953 (1995).

[25] T. Auguste, P. Monot, L.-A. Lompré, G. Mainfray, C. and Manus, Opt. Commun. **89**, 145 (1992).

[26] C.G. Durfee III and H.M. Milchberg, Phys. Rev. Lett. **71**, 2409 (1993).

[27] T. Ditmire, Phys. Rev. E **54**, 6735 (1996).

[28] M. Yamagiwa, J. Koga, A. Sagisaka, and K. Nagashima, Plasma Phys. Controlled Fusion **41**, 265 (1999).